



Stability of Oblique Water Entry of Cylindrical Projectiles

M. A. Akbari¹, J. Mohammadi^{2†} and J. Fereidooni¹

¹ Faculty of Mechanics, Malek Ashtar University of Technology, Iran

² Faculty of Aerospace, Malek Ashtar University of Technology, Iran

†Corresponding Author Email: mohammadijalal@mut.ac.ir

(Received April 6, 2020; accepted July 9, 2020)

ABSTRACT

Water entry is an interesting subject but many of its physical aspects have remained unknown so far. Using computational fluid dynamics (CFD), this study investigates the dynamic stability of cylindrical projectiles in the oblique water entry at shallow angles in the presence of three phases of air, water and water vapor. The three-dimensional and transient numerical model has been verified using the former experimental results in the literature. In this study, the effects of projectile length-to-diameter ratio (L/D) and water entry angle on the projectile stability within cavity were investigated. Accordingly, the water entry of six projectiles was simulated with aspect ratios of 2 to 6 at three water entry angles of 6, 9 and 12 degrees with respect to the free surface with an initial velocity of 280 m/s. At each of the aforementioned angles, the critical L/D , where the projectile avoids tumbling inside the cavity at a larger value, was determined. This study showed that in the oblique water entry of a cylindrical projectile at the angles of 6, 9 and 12 degrees, the projectile tumbled within the cavity with a L/D of less than 5, 4 and 3.5, respectively. The simulation results showed that increasing the L/D as well as the water entry angle relative to the free surface resulted in the improvement of the cylindrical projectile motion stability, which is in agreement with the experimental results. By analyzing the details of each simulation, it was found that the projectile stability within the cavity is correlated with the magnitude of the angular momentum which is generated in the projectile by the impact of the cavitator on the free surface and it was shown that the projectile with a specific L/D can withstand destabilizing angular momentum to a certain extent. Considering the fact that the atmospheric ballistics of gyroscopically stabilized projectiles lead to a limit for increasing L/D , this study showed that, for aluminum cylindrical projectiles in which air stability is achieved via the gyroscopic effect, the minimum water entry angle is 6° to attain the gyroscopic stability of the projectile in the air and stable motion inside the cavity. This fact is very important from a practical point of view.

Keywords Water entry; Cylindrical projectiles; Stability; Supercavitation.

NOMENCLATURE

C_x	axial force coefficient along the projectile axis	\mathbf{g}	earth's gravitational acceleration vector
D	cavitator and projectile diameter	I	moment of inertia
d	distance between the projectile center of mass and the location of exerted tail-slap normal force	L	projectile length
\mathbf{F}	external force vector exerted to the fluid	m_p	projectile mass
(f_x, f_y)	hydrodynamic force components exerted to the projectile along the projectile axis and normal to it (Fig.1)	\dot{m}_{qk}	mass transfer rate from phase q to phase k
(\hat{f}_x, \hat{f}_y)	hydrodynamic force components exerted to the cavitator along the projectile axis and normal to it (Fig.9 and 10)	\mathbf{M}	hydrodynamic moment vector exerted to the projectile
		M	moment exerted to the projectile with respect to Z direction (Fig.1)
		p	static pressure
		p_{sat}	saturation pressure
		p_{∞}	ambient pressure
		R	cavity radius
		R_c	cavity radius at the projectile tail (Fig.1)

\mathbf{V}	projectile velocity vector (Fig.1)		location
(V_x, V_y, V_z)	projectile velocity component along the inertial coordinate system axes	x_y	distance between the location of exerted tail-slap normal force and cavitator
(V_x, V_y, V_z)	projectile velocity component along the body coordinate system axes	θ, φ, ψ	the rotational angles of projectile with respect to the coordinate axis
(X, Y, X)	position of the center of mass of the projectile along the inertial coordinate system axes (Fig.10)	β	angle of attack (Fig.1)
(x, y, z)	position of the center of mass of the projectile along the body coordinate system axes (Fig.9)	ω	angular velocity
$x_{c.g}$	distance between the projectile center of mass and cavitator	$\alpha_l, \alpha_v, \alpha_a$	volume fraction of liquid, vapor and air phases
		ρ_l, ρ_v, ρ_a	density of liquid, vapor and air phases
		μ	dynamic viscosity
		ρ_w	water density

1. INTRODUCTION

Oblique water entry is defined as a structure which enters into the liquid phase (water) through free surface with an inclined angle with respect to the free surface. Oblique water entry is also an unsteady and nonlinear process involving multiphase flow (Hou *et al.* 2018). Perhaps the most important applications related to oblique water entry research are in the military industry (Bodily *et al.* 2014).

When high-speed structures move under water, cavitation can occur in a flow field if the static pressure is less than the vapor pressure. Cavitation can be defined as the formation of bubbles in a liquid subjected to local pressure reduction (Mirzaei *et al.* 2015). Supercavitating vehicles are high-speed underwater vessels which are fully enveloped by a cavity. Because only a small portion of the projectile in the cavitator actually contacts the liquid, the viscous drag on the projectile is considerably reduced when moving inside a supercavity.

Recently, numerous studies have focused on the vertical water entry in cylinders and wedge modes (Guo *et al.* 2012, Nguyen *et al.* 2014) but whenever the velocity vector of the projectile is no longer normal compared to the free surface, the dynamics of the projectile water entry problem may be dramatically altered. At shallow angles (5–15°), standard ballistic projectiles do not enter the water; instead, they ricochet off the surface or break into many pieces. Supercavitating projectiles which enter the water at shallow angles, are designed with blunt tips and large length-to-diameter ratios. These projectiles create a vaporous supercavity that originates at the tip of the bullet upon contact with the free surface (Truscott *et al.* 2009).

They are inherently unstable, as the hydrodynamic force acting on the cavitator almost always leads to a pitching moment on the projectile (akin to balancing a pen vertically on a flat table). Therefore, after successful water entry and because of this pitching moment, supercavitating projectiles may start to pitch up and down inside the cavity. Because of the pitching motion, the projectile tail may hit the cavity

wall. At this moment, there are two possible dynamic situations: 1) the projectile bounces back and impacts on the opposite side of the cavity (Fig. 1). This is known as the tail-slap phenomenon (Kulkarni *et al.* 2000); or 2) the tail-slap cannot provide the righting moment required to return the projectile into the cavity and the projectile pitch angle keeps increasing constantly and eventually, the projectile tumbles inside the cavity.

Previous experiments have revealed that projectiles with flat cavitators and high length-to-diameter ratios (L/D) can enter the water through the free surface at shallow angles and continue moving inside supercavity without ricocheting (Hrubes 2001). The experiments explained that these types of projectiles are stabilized underwater through tail-slap (Hrubes 2001) (i.e., Tail-slap can produce a righting moment big enough to push the projectile back into the cavity). It should be noted that projectiles with a large L/D have a longer moment arm for the righting moment and hence, an improved stability.

In the case of larger L/Ds, a higher longitudinal spin rate is needed to achieve gyroscopic stability in the air. McCoy indicated that in atmospheric ballistics of gyroscopically stable projectiles, the maximum L/D should not exceed 5~6 and in higher values, the spin rate required for aerodynamic stability may be unfeasibly large (McCoy 1999). This presents a challenge for air-to-water ballistic applications. The most difficult part of the problem is to find the right L/D value for both aerodynamic and hydrodynamic stabilities. Therefore, the primary aim of the present study is to investigate the relationship between the aforementioned subjects.

Truscott *et al.* demonstrated stable air-to-water flight for spinning projectiles with a relatively small L/D at shallow water entry angles (Truscott *et al.* 2009). Truscott revealed that bullets with lower length-to-diameter ratios tumble inside the cavity, while higher length-to-diameter ratios can mitigate the tumbling behavior. While Truscott's data presented herein are specific to 0.22 caliber bullets, he showed that the findings can be readily extended to higher speed and higher caliber projectiles. However, in Truscott's research, the minimum L/D in which the cylindrical

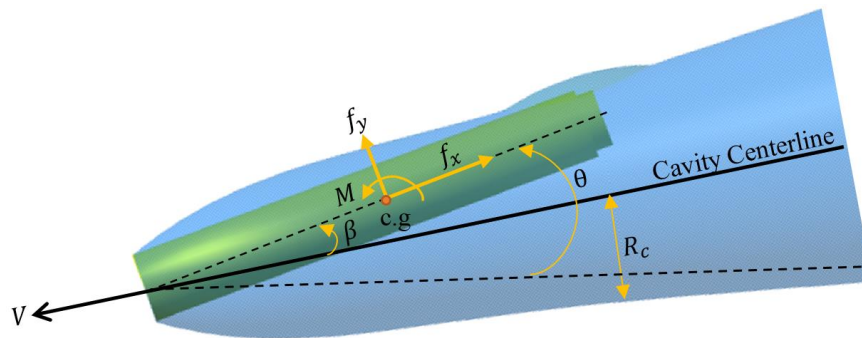


Fig. 1. Schematic of the tail-slap phenomenon and different geometrical parameters of a supercavitating projectile.

projectiles avoid tumbling is not explicitly mentioned.

The forces generated during initial moments of water entry and water impact problems can be significantly large and vary according to the angle of entry, shape of the cavitator, surface properties, impact velocity and fluid properties such as viscosity, density and surface tension (Derakhshanian *et al.* 2018). Therefore, prediction of subsequent projectile motion is absolutely difficult due to fluid-solid interactions, especially when unexpected phenomena such as tail-slap occur (Rabiee *et al.* 2011). In recent years, a more precise simulation of the oblique water entry problem has become possible. Computational Fluid Dynamics (CFD) is a flexible and powerful tool for establishing an accurate model to simulate water-entry events. Numerical results give us an effective point of view for understanding the complex water-entry process.

Main numerical studies on water entry concentrated on vertical entry via a axisymmetric or two-dimensional model (Nguyen *et al.* 2016, Iranmanesh *et al.* 2017), and few studies have been conducted to investigate oblique water entry. The number of numerical studies which can be quantitatively validated against experiment is very limited. (Chen *et al.* 2019a) considered the oblique water entry impact of three different cylindrical geometry vehicles with the same lengths but different cavitator diameters experimentally and numerically (Chen *et al.* 2019a). Chen applied the commercial code ANSYS Fluent and Reynolds-averaging Navier-Stokes (or RANS) equations (Chen *et al.* 2019a). Hou *et al.* investigated characteristics of oblique water entry of a cylinder with a relatively low speed by employing numerical and experimental methods. They used a sliding mechanism in which the projectile slides and then falls into the fluid with a relatively low initial speed which is sped up later by means of gravitational force. Hou constructed the 6DOF numerical model by using the volume of fluid (VOF) method, the large eddy simulation (LES) approach and the Eulerian multiphase model to simulate water entry physics. Gao *et al.* (2019) investigated the dynamics of high-speed oblique water entry of different cylindrical projectiles with different initial conditions. They showed that at shallow entry angles, the projectile hits the cavity

wall and makes the cavity wall less smooth and with the increase of the entry angle, it becomes possible to provide stability for the projectiles inside the cavity. They have also shown that oblique water entry of projectiles with small L/D will end up in a ricochet. (Chen *et al.* (2019b)) studied the influences of entry angle, entry speed and cavitator area on the axial force of three types of vehicles with a disk cavitator experimentally and numerically. Their article investigated the axial force which is exerted on the projectile at entry process and attempted to figure out a relationship between the peak axial force and other entry parameters.

It is obvious that studying cylindrical projectiles will enhance the scientific understanding of the oblique water entry problem. In this study, we have simulated high-speed oblique water of six particular cylindrical projectiles impacting the free surface at shallow entry angles. Projectiles have the same initial velocity. Special attention is given to the minimum L/D and the entry angle for each projectile and also determining whether or not the projectiles tumbled after the entry. The aforementioned topics have not been fully investigated in any previous researches.

Numerical simulation is performed using the commercial CFD software code STAR-CCM+ to solve the main equations. The numerical model is validated using results from Truscott's experiments (Truscott *et al.* 2009).

This study examines unexplored areas, and by combining the results of this study with the results from previous experiments (Truscott *et al.* 2009), a more detailed description of the stability conditions of cylindrical projectiles in the high-speed oblique water entry will be obtained.

2. NUMERICAL METHODOLOGY

2.1 Governing equations of fluid flow

The governing equations, including the standard Navier-Stokes, volume fraction and turbulence equations, are used to solve velocity and pressure parameters throughout the domain. The equation of fluid flow has the following form:

$$\frac{\partial}{\partial t}(\rho \mathbf{V}) + \nabla \cdot (\rho \mathbf{V} \mathbf{V}) = -\nabla p + \nabla \cdot [\mu(\nabla \mathbf{V} + \nabla \mathbf{V}^T)] + \rho \mathbf{g} + \mathbf{F} \quad (1)$$

In multiphase flow field, sharp interfaces can be tracked by solving the continuity equation for the volume fraction of the second phase. For the q^{th} phase, the equation has the following form:

$$\frac{\partial}{\partial t}(\rho_q \alpha_q) + \nabla \cdot (\rho_q \alpha_q \mathbf{V}_q) = \sum_{k=1}^n (\dot{m}_{kq} - \dot{m}_{qk}) \quad (2)$$

Where ρ is the fluid's density, α represents the volume fraction, \dot{m}_{qk} is the mass transfer rate from phase q to phase k , and \mathbf{V} is the fluid's velocity. In order to close the equations in the unsteady Reynolds-averaged Navier-Stokes (URANS) method, the two-equation turbulence model SST $k-\omega$ was applied to simulate the effects of turbulence in the flow field.

Yuan *et al.* (2017) have shown that in the case of open cavity, which is formed during the entry process of a projectile, large amounts of air can enter the cavity. Accordingly, there are three phases of water, vapor and air during the high-speed oblique water-entry process. Therefore, the three-phase model would be more appropriate for this paper. A review of the reported literature indicates that the VOF technique is in accordance with natural cavitation physics and can accurately capture the shape and characteristics of a cavity (Aus der Wiesche 2005). Passandideh-Fard and Roohi (Passandideh-Fard *et al.* 2008) indicated that the VOF technique is a more accurate method to simulate the natural cavitation. Therefore, the VOF interface tracking method (Hirt *et al.* 1981) is used to simulate interactions between the three phases. In the VOF approach, the dynamic viscosity and the fluid density are defined as:

$$\mu_m = \mu_l \alpha_l + \mu_v \alpha_v + \mu_a \alpha_a \quad (3)$$

$$\rho_m = \rho_l \alpha_l + \rho_v \alpha_v + \rho_a \alpha_a \quad (4)$$

$$\alpha_l + \alpha_v + \alpha_a = 1 \quad (5)$$

Where ρ_m, ρ_a, ρ_l and ρ_v are the density of mixture, air, liquid and vapor, μ_m, μ_a, μ_l and μ_v are the viscosity of mixture, air, liquid and vapor, and α_l and α_v are the volume fraction of liquid and vapor, respectively.

The cavitation was modelled using the Schnerr-Sauer cavitation model which is based on the Rayleigh-Plesset equation (Schnerr *et al.* 2001). Therefore, this cavitation model can be used for mass transfer simulation between the liquid and vapor phases. Within the cavitation process, the equation for the vapor volume fraction has the following form (Zwart *et al.* (2004), Yu *et al.* (2019)):

$$\frac{\partial}{\partial t}(\rho_v \alpha_v) + \nabla \cdot (\rho_v \alpha_v \mathbf{V}_v) = \frac{3}{R} \sqrt{\frac{2(p_v - p_\infty)}{3}} \frac{\rho_v \rho_l}{\rho_m} \alpha_v (1 - \alpha_v) \quad (6)$$

$$R = \left(\frac{\alpha_v}{1 - \alpha_v} \frac{3}{4\pi} \frac{1}{2} \right)^{1/3} \quad (7)$$

2.2 Projectile Equations of Motions

To examine rigid body (projectile) dynamics in three-dimensional space, Newton's second law must be extended to define the relationship between the movement of the projectile and the system of forces and torques that act on it. The projectile equations of motions can be described as follows:

$$\frac{d\mathbf{V}}{dx} = \frac{\Sigma \mathbf{F}}{m_p} \quad (8)$$

$$\frac{d\omega}{dt} = \frac{\Sigma \mathbf{M}}{I} \quad (9)$$

$$\dot{X} = V_x, \quad \dot{Y} = V_y, \quad \dot{Z} = V_z \quad (10)$$

$$\dot{\theta} = \omega_z, \quad \dot{\phi} = \omega_y, \quad \dot{\psi} = \omega_x$$

Where $[X, Y, Z]$ and $\mathbf{V}=[V_x, V_y, V_z]$ are the position of the center of mass and velocity vector of the projectile, respectively. \mathbf{M} and \mathbf{F} are the moments and force vector acting on the projectile respectively, and m_p and I are the mass and moment of inertia of the projectile, respectively. $[\theta, \phi, \psi]$ are the rotational angles and ω is the angular velocity of the projectile.

2.3 Boundary Conditions and Mesh Generation

In the present study, the commercial computational fluid dynamics code STAR-CCM+ was used to perform the simulation which is based on the finite volume method (FVM). In order to simulate the free surface above water column, two different types of fluids (i.e. water and air) and three different flow phases (i.e. liquid, vapor and air) had to be modelled. While the free surface was defined between the water and air, a multiphase interaction was described between the liquid and vapor phases of the water for modelling cavitation. In the STAR-CCM+ code, the static water surface can be defined by the VOF wave model. Hence, the interface of gas and liquid phases can be defined and captured in the simulation. Overlap grid and 6DOF dynamics were also used to simulate the process of water entry.

It is important that the value of the Courant number is less than 1. Therefore, in the present study, the simulation time step is set to 10^{-7} seconds. In the present study, the second-order implicit scheme was used to discretize the diffusion and convection terms of the governing equations and VOF model. In the code, the Segregated Flow solver based on the SIMPLE algorithm can couple flow field pressure and velocity.

Fig. 2(a) depict the numerical boundary conditions (BCs) which are applied in this study. The physics of the problem implies that the velocity BC at the inlet is zero and the pressure BC at the outlet is relative to static pressure which depends on the water column height. The overset mesh BC is used for the boundary of the overlap grid, as shown in Fig. 2(b). To achieve high-quality grids, the trimmer mesher model, the prism layer mesher model and the surface remesher model on the wall BC are employed as shown in Fig. 2(b). In addition, the grid of the projectile trajectory, the overset area and water surface are refined to enhance the computational quality as shown in Fig. 2(b)

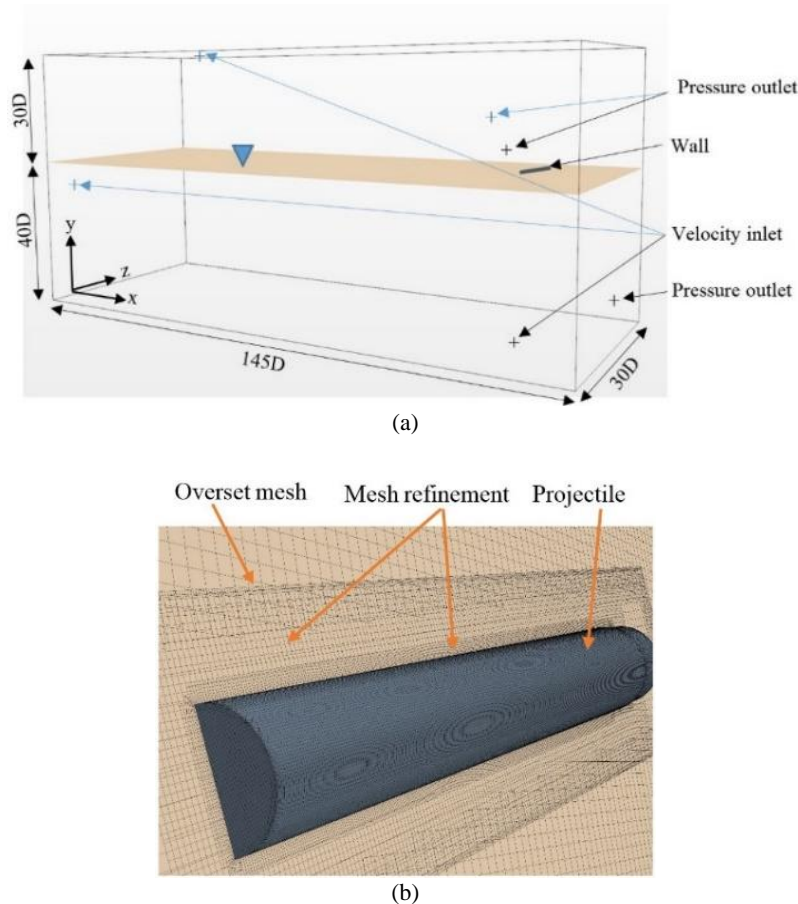


Fig. 2. (a) Diagram of computational domain (D is the diameter of cylinder), (b) the computational mesh on a plane section and some details about overset mesh.

2.4. Grid Independent Study

In this section, a grid convergence study has been conducted based on the oblique water entry of a specific cylindrical projectile, using three different grid levels with correspondingly coarse (1.5 million), medium (2.1 million) and fine (2.75 million) grids. Figure 3(a-c) shows the change in the predicted horizontal velocity of the cylinder, total pitching moment and the angular velocity of the cylinder, respectively. These figures indicate that time histories of projectile velocity with different grid levels are not very different from each other while the projectile angular velocity is considerably different from that obtained with coarse grids. Considering the accuracy of results, the medium one with 2.1 million grids is used in the following studies.

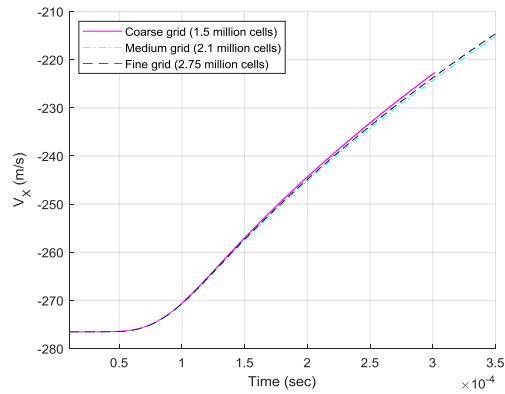
2.5 Validation of Applied Numerical Method

In order to validate the numerical method, a previously experiment within literature (Truscott *et al.* 2009), with 5.51 mm tip diameter and cylindrical shape (MIT Slug) was simulated and numerical and experimental results have been compared with each other. In Fig. 4, the cavity evolution, entry water splash, the free surface reaction, tail-slap and tail-

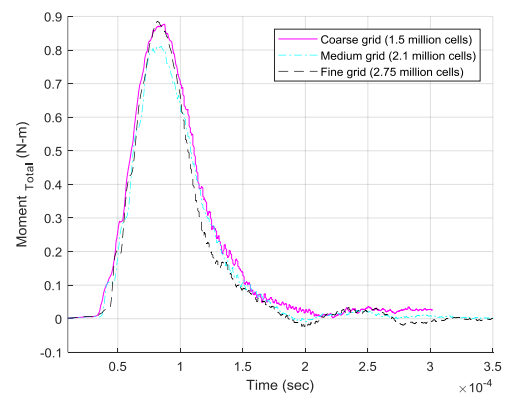
slap water splash from simulations are compared with the experiment illustrations (Truscott *et al.* 2009). It can also be clearly seen that the results of the water entry events for both studies are in total agreement with each other. The comparison of time histories of horizontal velocity component, angular velocity and axial force of the projectile obtained by numerical simulation and experiment results is shown in Fig. 5 (a-c), respectively. It can be seen that our results agree with the experiment results, and consequently it is expected that the present numerical method can simulate the oblique water entry problems with decent accuracy.

3. RESULTS AND DISCUSSION

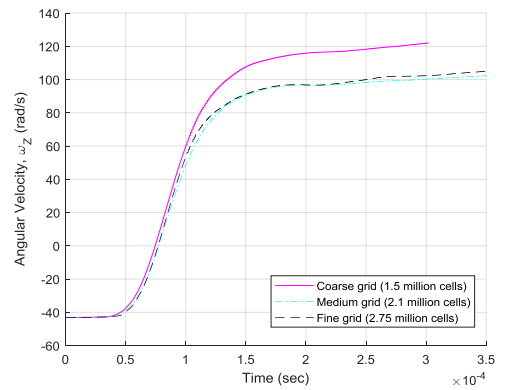
In this section, the motion stability of the cylindrical projectile in the oblique water entry is investigated. In the first part, the water entry of six cylindrical projectiles with a L/D between 2 and 6 is modeled and the critical L/D is determined for three water entry angles of 6, 9 and 12 degrees. In the second part, by extracting the details of each simulation, the reasons for projectile instability within the cavity will be explained. In this section, the effect of L/D and the water entry angle on the stability of the projectile within the cavity is also examined.



(b)



(b)



(c)

Fig. 3. Time histories of (a) horizontal components of velocity V_x , (b) total moment M and, (c) angular velocity ω_z with three different grid levels.

Table 1 presents the geometry and mass characteristics of the projectiles related to this study. All simulated projectiles have a diameter of 5.51 mm and are made of aluminum with a density of 2700 kg/m³. All projectiles at the start of the motion have no angular velocity and angle of attack, and they have an initial velocity of 280 m/s.

3.1 The Critical L/D at Different Water Entry Angles

Initially, the projectiles with different L/D values

were investigated at a specific water entry angle of 9° with respect to the free surface, and the minimum L/D in which the projectile will keep the stability within the cavity was extracted. For determining the critical L/D at the angles of 6° and 12°, four separate simulations have been conducted according to the information presented in Table 1.

Table 1 Geometric and mass properties of the projectiles used in the simulation and their related water entry angle

L/D	Mass (g)	Water entry angle (deg.)	Projectile shape
6	2.13	9	[Redacted]
5	1.77	6 & 9	[Redacted]
4	1.42	6 & 9	[Redacted]
3.5	1.24	9	[Redacted]
3	1.06	9 & 12	[Redacted]
2	0.70	12	[Redacted]

The projectile water entry and cavity formation at angles of 9°, 6° and 12° are shown in Figs. 6-8, respectively.

Figs. 6-a through 6-e show the projectile water entry with L/D values of 6 through 3, respectively at a 9° water entry angle. As can be seen, as the L/D decreases, the straight-line trajectory of the projectile is converted to a curved line.

As shown in Fig. 6-a, for the projectile with L/D = 6, there is no tail-slap at t = 1ms whereas according to Fig. 6-b, for the projectile with L/D = 5, tail-slap occurred at t = 1ms. Therefore, it can be deduced that as the L/D decreases, tail-slap occurs within a shorter time duration.

Unlike projectiles with L/D ≥ 4 (Fig. 6-c), projectiles with L/D = 3 and L/D = 3.5 (Fig. 6-d and Fig. 6-e) are tumbled when the projectile body collides with the cavity wall and hence, instability was observed. Therefore, the critical L/D of the cylindrical projectile at 9° entry angle is estimated to be in the range of 3.5 < (L/D)_{cr} < 4.

As can be seen in Fig. 6-e, the colliding of the lateral surfaces of the projectile with the cavity wall occurs in a way that the location of the total force applied by the collision is closer to the cavitator relative to the projectile center of the mass. In such a situation, the tail-slap not only has not prevented the projectile from tumbling within cavity, it has also acted as an unstabilizing moment. In the following sections, this phenomenon will be discussed in detail.

According to the results of 9° water entry, it can be expected that by decreasing the entry angle, the critical L/D occurs in relatively large quantities. Therefore, based on this, the water entry of projectiles with L/D = 4 and L/D = 5 is simulated at a water entry angle of 6°. In Fig. 7, some results of this simulation are shown at certain time intervals.

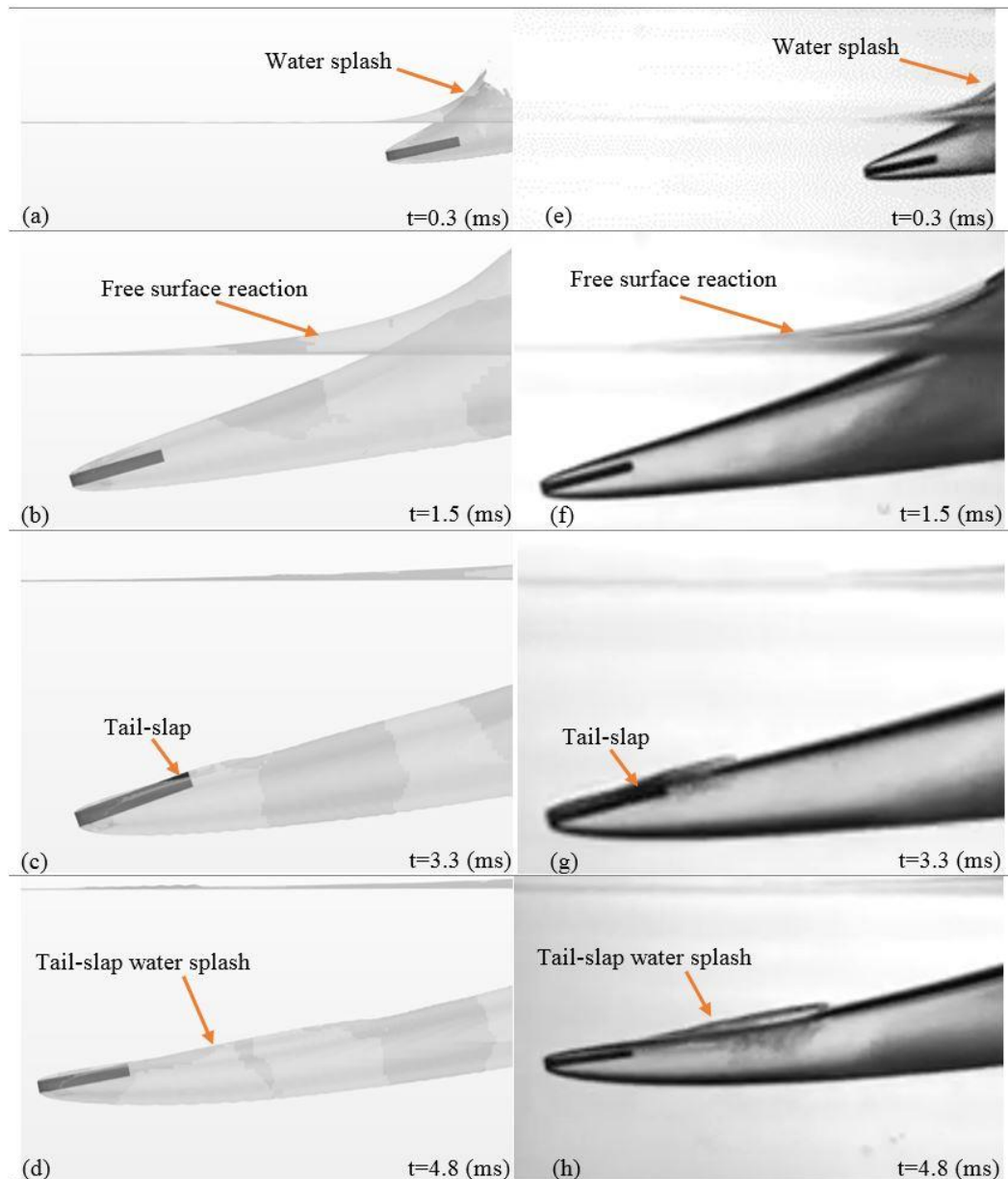


Fig. 4. Comparison of the cavity evolution and water entry events between numerical simulation (a-d) and experiment result (e-h) (Truscott *et al.* 2009).

Based on Fig.7-a, in the projectile with $L/D=5$ and after the slapping event, the pitch angle has decreased and the projectile has returned into the cavity and therefore, the projectile exhibits stable dynamics inside the cavity. In Fig. 7-b, however, the projectile pitch angle with $L/D = 4$ did not decrease after colliding with the cavity and the pitch angle continuously increased. Thus, the critical L/D at the 6° entry angle occurs in the range of $4 < (L/D)_{Cr} < 5$.

Based on the physics involved in this problem, by increasing the water entry angle from 9 to 12 degrees, it is expected that the stability of the cylindrical projectiles will occur at lower L/D values in comparison to 9° entry angle. Therefore, two projectiles with $L/D = 2$ and $L/D = 3$ were selected as candidates for modeling the 12° water entry angle.

According to Fig. 8b, the projectile with $L/D = 2$ tumbles while the projectile with the $L/D = 3$ keeps its stability and its pitch angle decreases after the tail-slap. Therefore, at the 12° entry angle, a tumbling occurs in the range of $2 < (L/D)_{Cr} < 3$.

The overall results of the simulation data are presented in Table 2. The critical value of L/D at each water entry angle will occur between stable and unstable limits which is shown with blue cells in Table 2. As can be seen in Table 2, in order to sustain projectile stability inside the cavity, both the L/D value and the entry angle need to be increased.

It is clear that as the value of L/D increases, a larger longitudinal spin rate is needed to achieve gyroscopic stability in air. McCoy indicated that in

atmospheric ballistics of gyroscopically stable projectiles, the maximum L/D should not exceed 5~6 and in higher values, the spin rate required for aerodynamic stability may be unfeasibly large (McCoy 1999). Based on the aforementioned issues and the information presented in Table 2, it can be concluded that aluminum cylindrical projectiles in which air stability is achieved using the gyroscopic effect, a water entry angle of 6° is the minimum water entry angle to achieve projectile's stable motion inside the cavity and this fact is very important from a practical point of view.

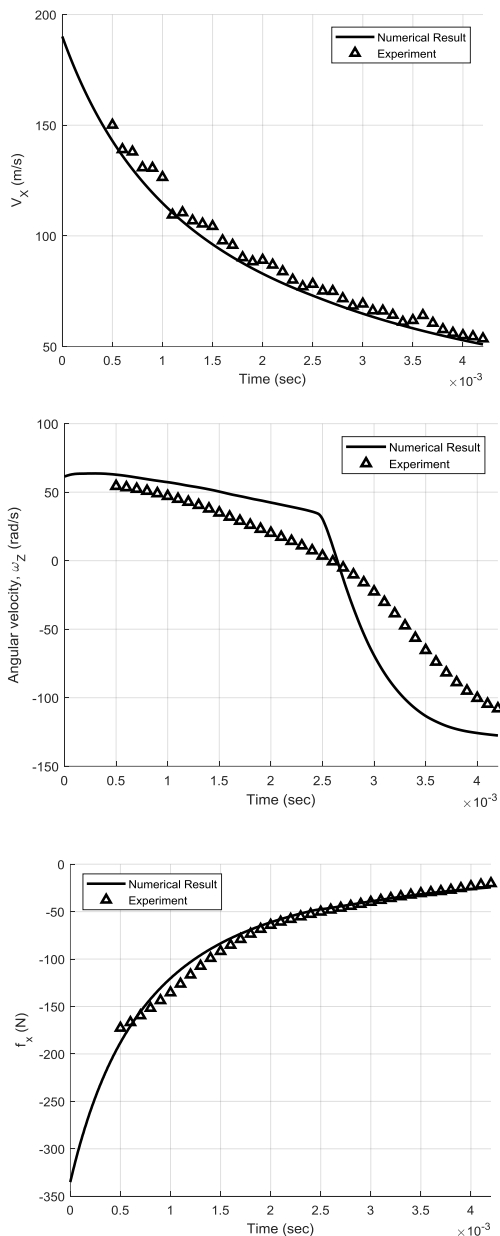


Fig. 5. Comparisons of (a) horizontal components of velocity V_x , (b) angular velocity ω_z and (c) axial force f_x between the experiment (Truscott *et al.* 2009) and numerical simulation.

Table 2 General results of water entry simulation of cylindrical projectiles at different angles

L/D	2	3	4	5	6
6 (deg)	-	-	×	√	-
9 (deg)	-	×	√	√	√
12 (deg)	×	√	-	-	-

√: Stable ×: Tumbled -: Non simulated

3.2. Analyzing the Reasons for Projectile Instability Within the Cavity

In this section, details of the projectile water entry dynamics have been extracted and the reasons behind the projectile instability within the cavity are discussed. Special attention is given to the effect of change in L/D on the projectile dynamics at a certain water entry angle of 9° .

In order to extract the dynamics of the projectile, two independent coordinate systems have been selected. Figure 9 shows the position of the body's origin of the coordinate system which is attached to the projectile center of mass, and Fig. 10 shows the position of the origin of the inertial coordinate system which is matched to the projectile center of mass at the starting point.

Schematics of the forces applied to the projectile cavitator are shown in Figs. 9 and 10 while it makes contact with the free surface and when it moves inside the cavity, respectively. The details of these forces will be discussed later. It is also worth noting that the results of unstable projectile dynamics are shown by dashed lines in all the graphs presented in this section.

3.2.1 The Effect of L/D on Projectile Stability

In Figs. 11 and 12, the position of the center of mass and the pitch angle of the projectile at an entry angle of 9° in the inertial coordinate system are shown, respectively. As shown in Fig. 11, it is evident that as the value of L/D decreases, the curvature of the projectile's path (deviation from the straight-line path) is increased. Therefore, it is expected that increasing the L/D will improve the path of the projectile to the straight-line within the cavity. As shown in Fig. 12, the projectiles with $L/D = 3$ and $L/D = 3.5$ tumble within the cavity and become unstable. In this case, tail-slap was unable to prevent the projectile pitch angle from increasing.

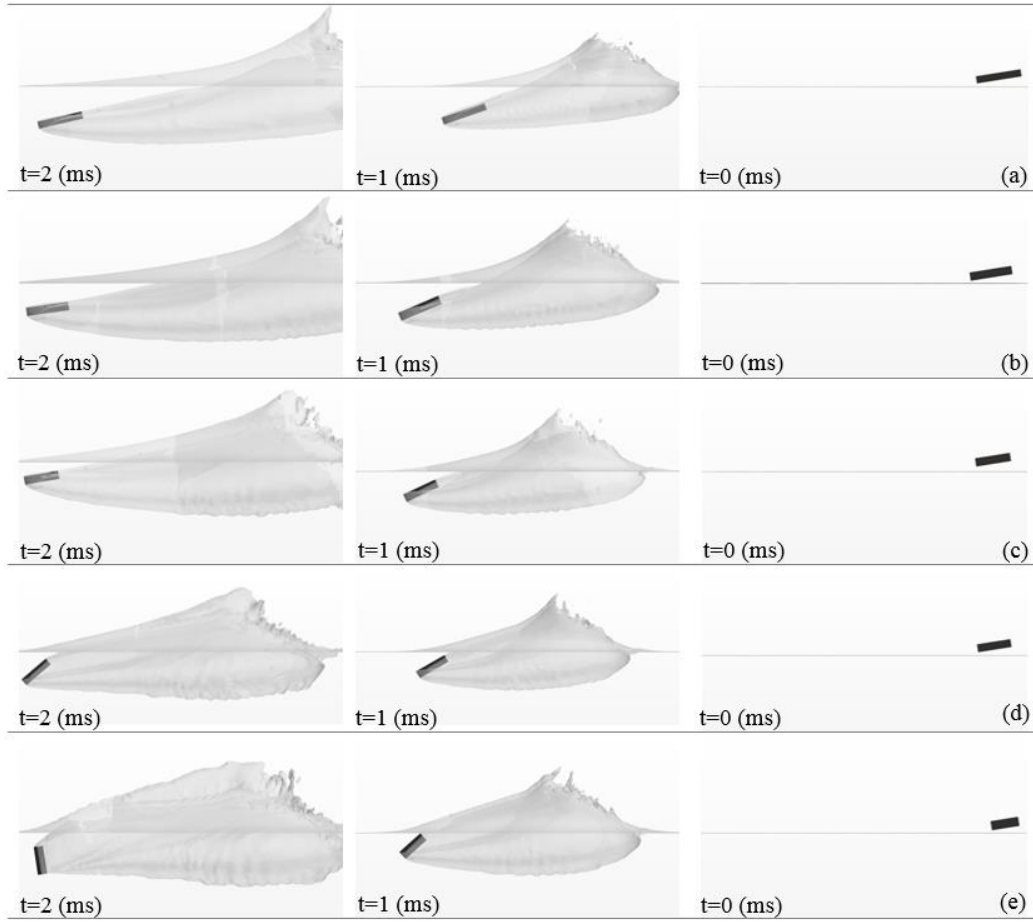


Fig. 6. Projectile water entry at an angle of 9° with respect to the free surface; a) $L/D = 6$, b) $L/D = 5$, c) $L/D = 4$, d) $L/D = 3.5$ and e) $L/D = 3$.

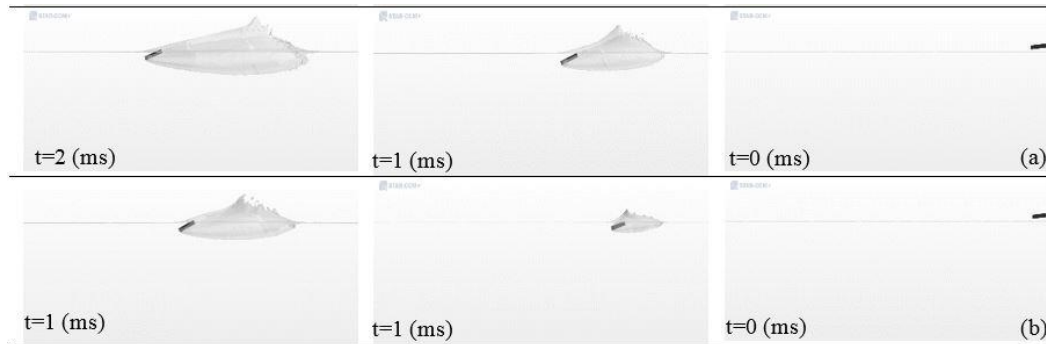


Fig. 7. Projectile water entry at an angle of 6° with respect to the free surface; a) $L/D = 5$, b) $L/D = 4$.

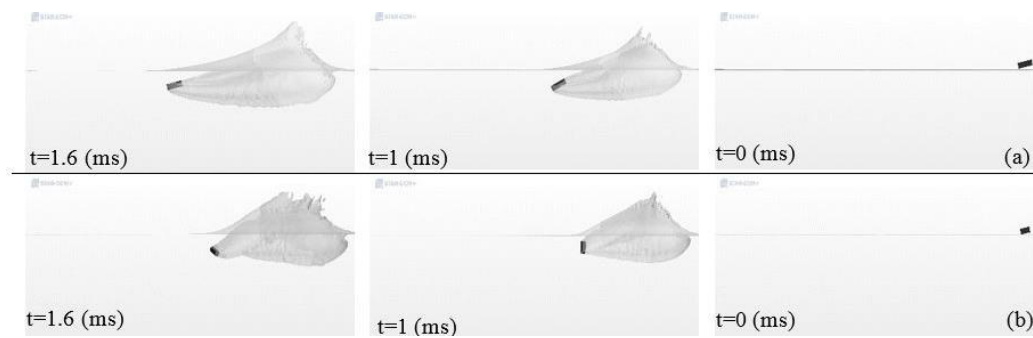


Fig. 8. Projectile water entry at an angle of 12° with respect to the free surface; a) $L/D = 3$, b) $L/D = 2$.

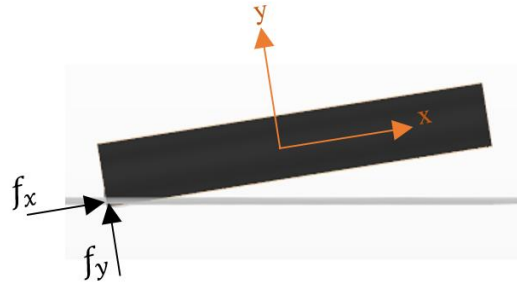


Fig. 9. Position of the body’s origin of the coordinate system and the schematic of the force applied to the projectile while making contact with the free surface.

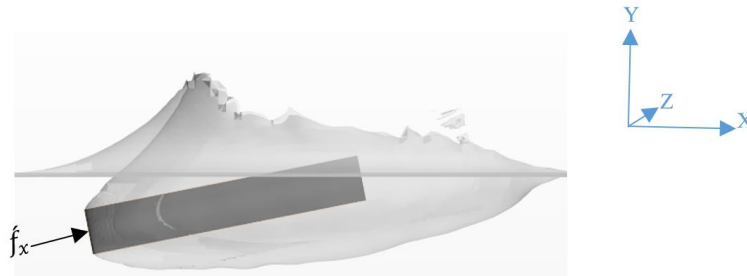


Fig. 10. Position of the origin of the inertial coordinate system and the schematic of the force applied to the projectile after the water entry.

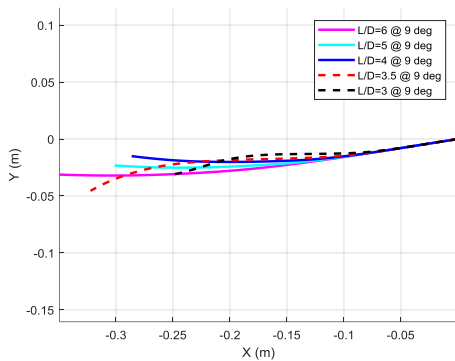


Fig. 11. Projectile’s center of mass position at a 9° water entry angle with respect to the free surface.

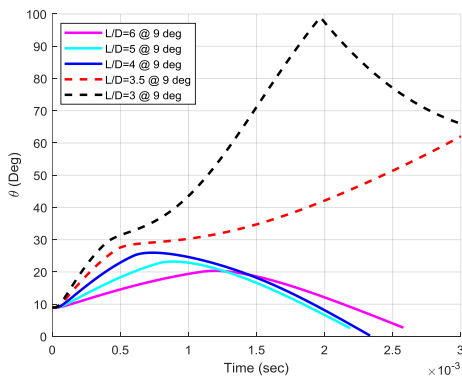


Fig. 12. Projectile’s pitch angle at a 9° water entry angle with respect to the free surface.

According to Eq. 11 (Kiceniuk, 1954), the axial force applied to the projectile depends on the diameter of

the cavitator and the projectile velocity. Since the cavitators are identical in all projectiles, it is expected that the axial force applied to the projectile, resulting from making contact with the free surface, will be approximately the same for projectiles which have different L/D values.

$$f_x = C_x \left[\frac{1}{2} \rho_w V^2 \left(\frac{\pi}{4} D^2 \right) \cos \beta \right] \quad (11)$$

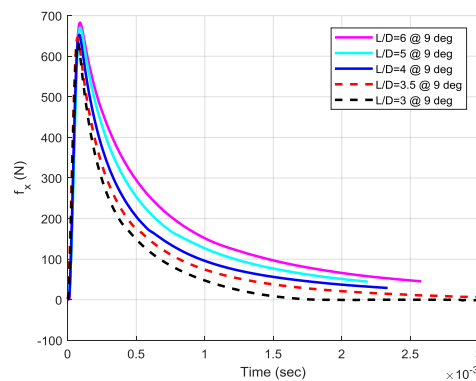


Fig. 13. Diagram of force applied along the projectile axis at a 9° water entry angle with respect to the free surface.

Figures 13 and 14 show the forces applied to the projectile in the body coordinate system. Accordingly, when the projectile makes contact with the free surface, the force magnitude on the projectile increases dramatically. For projectile water entry with L/D = 6, the maximum axial and normal forces are +680 and -22 N, respectively and the maximum axial and normal force applied to the projectile with

$L/D = 3$ are 650 and -21 N, respectively. So, by doubling the value of L/D , the maximum force applied to the projectile after making contact with the water surface will only increase by 5%. Therefore, it can be concluded that changing the value of L/D (within the range investigated in this study) has little effect on the maximum force applied to the projectile when making contact with the water surface.

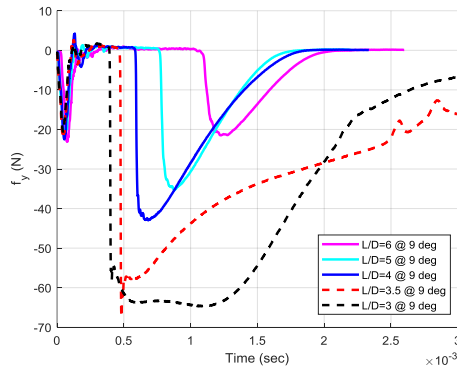


Fig. 14. Diagram of applied normal force to the projectile axis at a 9° water entry angle with respect to the free surface.

According to Figs. 9 and 10, the status of the forces applied to the projectile at the water entry can be divided into two distinct stages. In the first stage, making contact with the free surface results in two axial and normal force components at the collision point which leads to an unstabilizing pitching moment for the projectile due to the resultant force being applied to a location out of the disk center. In the second stage, the projectile is completely covered by the cavity and the only force exerted by the fluid is perpendicular to the cavitator and its location corresponds to the center of the disk. In the second stage, no pitching moment is applied to the projectile, and the resultant force on the cavitator is schematically shown in Fig. 10. Based on Fig. 14, the normal force component (f_y) gradually disappears after the formation of cavity and before the tail-slap event. Therefore, it can be concluded that in the second stage, the only force applied to the cavitator is the axial force (f_x) along the projectile axis which is consistent with previous findings (Kiceniuk (1954)).

In the second stage, the tail-slap results in a normal force which is applied to the projectile body. As shown in Fig. 14, as L/D decreases, the magnitude of the tail-slap normal force is increased. The highest tail-slap normal force is related to the projectiles with $L/D = 3$ and $L/D = 3.5$, nevertheless, the projectiles have tumbled inside the cavity. The moment applied to the projectile, which was influenced by the normal force applied to it (f_y), is calculated as follows:

$$M = f_y \cdot d \quad (12)$$

$$d = x_y - x_{c.g} \quad (13)$$

According to Eq. 13, the reason behind the projectile tumbling within the cavity can be attributed to the change in location of the body normal force, to a point somewhere closer to the cavitator than the projectile's center of the mass and consequently, the

unstabilizing moment on the projectile. By exploring the projectile moment diagram, this phenomenon can be discussed more precisely.

Figures 15 and 16 represent the moment applied to the projectiles and the angular velocity which is generated in the projectile by the entry moment, respectively. According to Fig. 15, making contact with the free surface and applying asymmetric forces on the cavitator results in an initial unstabilizing moment. This moment, in accordance with the inertial moment, generates a different level of maximum angular velocity in the projectiles.

Based on Fig. 16, the entry moment for the projectiles with $L/D = 3$ and $L/D = 6$ provides maximum angular velocity of 1180 and 220 rad/s, respectively. Therefore, as the L/D increases, the angular velocity decreases because of increasing their inertia moments.

As the projectile moves along the motion path and while the tail-slap event occurs, stabilizing moment is applied on the projectile in the opposite direction compared to the initial unstabilizing moment which reduces the angular velocity of the projectile. As shown in Fig. 15, a similar dynamic behavior is observed in all stable projectiles except for the projectiles with $L/D = 3.5$ and $L/D = 3$.

As shown in Fig. 15, for the projectiles with $L/D = 3$ and $L/D = 3.5$, there is a difference in the applied moment dynamic compared to the other projectiles. Unlike other projectiles, unstabilizing moment is applied on the projectiles with $L/D = 3$ and $L/D = 3.5$ within the time range of 0.5 to 1.5ms. However, the normal force resulting from colliding with the cavity wall is in the line with the other projectiles. In the projectiles with $L/D = 3$ and $L/D = 3.5$, the normal force which results from the collision between the projectile body and the cavity wall is applied at a closer distance to the cavitator relative to the center of mass and, thus, unstabilizing collision moment increases. As shown in Fig. 16, the angular velocities of projectiles with $L/D = 3$ and $L/D = 3.5$ increase from 280 and 60 rad/s, to 1100 and 403 rad/s respectively which ultimately leads to the tumbling of the projectiles inside the cavity.

The unstabilizing moment on the projectile with $L/D = 3$ can be seen in Fig. 15. As can be seen, the unstabilizing moment increased up to 0.04 N-m in the time range of 0.5-1.5ms. However, in the stable projectiles, there is no unstabilizing moment while the tail-slap event.

According to Fig. 15, the moment which is applied to the projectiles in the flow formation phase is not much different, but higher values of pitching moment belong to the projectiles with higher aspect ratios. According to Eq. 14, the moment integral over the time leads to a change in the magnitude of the angular momentum of the projectile. This can be seen in Fig. 17. Therefore, projectiles with a higher aspect ratio have a larger angular momentum, so much so that when the L/D value is doubled, the $I\omega$ value increases by 48.8%.

$$\int M dt = I\Delta\omega \quad (14)$$

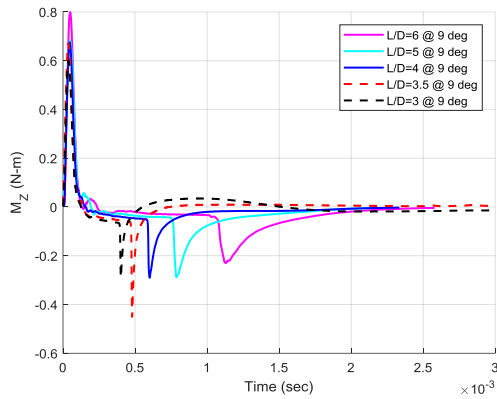


Fig. 15. Moment applied on the projectiles at a 9° water entry angle with respect to the free surface.

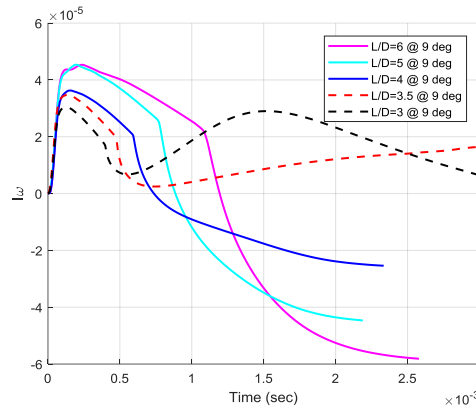


Fig. 17. Projectile angular momentum at a 9° water entry angle with respect to the free surface.

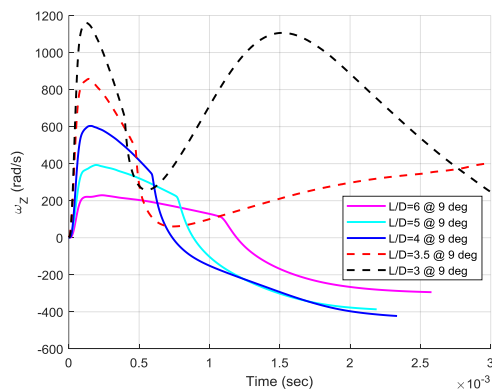


Fig. 16. Angular velocity created in the projectile at a 9° water entry angle with respect to the free surface.

The diagram of angular momentum of the projectiles is shown in the Fig. 17 at a 9° water entry. Based on this figure, it is evident that the water entry process causes an unstabilizing angular momentum on the projectile. The tail-slap generates a stabilizing angular momentum which results in the returning of the stable projectile into cavity. As a result, the stability of motion within the cavity can be determined by comparing these angular momentums.

Figure 17 shows that for all projectiles, the angular momentum has a positive value due to the impact of the projectile on the free surface. As the projectile moves along the direction path, the collision between the projectile body and the cavity wall decreases the angular momentum. The angular momentum in the projectiles with $L/D = 3$ and $L/D = 3.5$, which is a result of colliding with the cavity wall, cannot overcome the initial angular momentum to make it zero and then negative. Therefore, the projectile pitch angle increases continuously and ultimately, the projectile tumbles within the cavity.

Based on Fig. 17, the tail-slap stabilizing angular momentum increases with the increase in L/D . Therefore, higher value of L/D has a great effect in controlling the initial unstabilizing angular momentum.

Figure 18 shows the dimensionless axial force coefficient (C_x) of the projectile which is defined by Eq. 11. As can be seen, the value of C_x sharply increases while the projectile makes contact with the free surface and its value does not change with the change of L/D . For all projectiles, the axial force coefficient is estimated to be 0.83 after cavity formation, which is in agreement with the previous results in the literature (Mirzaei *et al.* (2015)). As the tail-slap occurs, the small reduction in C_x occurs at L/D values of 6, 5 and 4. Instability makes a further reduction in C_x value in the projectiles with $L/D = 3$ and $L/D = 3.5$.

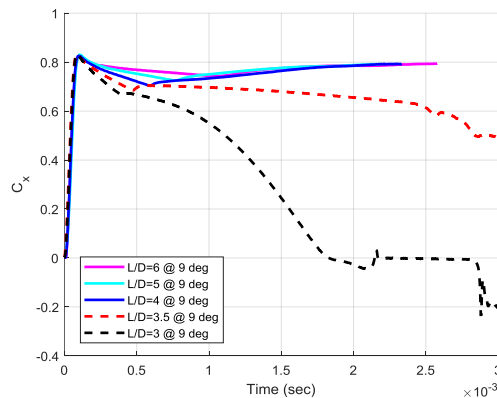


Fig.18. Projectile axial force coefficient at a 9° water entry angle with respect to the free surface.

3.2.2 Analyzing the Effect of Water Entry Angle on Projectile Stability

Figs. 19 and 20 show the moment and angular velocity changes at two water entry angles of 6 and 9 degrees for the projectile with $L/D = 4$. According to these diagrams, with a decrease in water entry angle with respect to the free surface, the initial angular momentum resulting from the projectile collision with the free surface has increased. According to Fig. 19, this increase is most likely because of the increase in the duration of moment applied to the projectile due to making contact with

the free surface.

As seen in Fig. 20, as the water entry angle decreases, the initial angular velocity, which is generated in the projectile due to making contact with the free surface, increases from 600 to 780 rad/s.

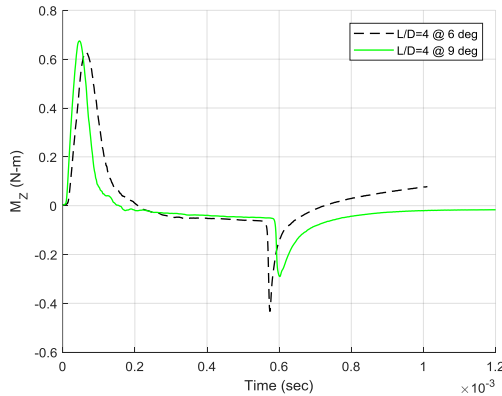


Fig. 19. Moment applied to the projectile with $L/D = 4$ at water entry angles of 6 and 9 degrees.

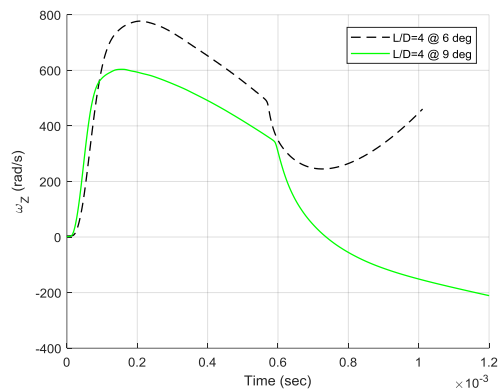


Fig. 20. Angular velocity of the projectile with $L/D = 4$ at water entry angles of 6 and 9 degrees.

4. CONCLUSION

This study investigated the dynamic stability of cylindrical projectiles in the oblique water entry at shallow angles in the presence of three phases of air, water and water vapor. The three-dimensional and transient numerical model has been verified using the former experimental results in the literature. In this study, the effects of projectile's length-to-diameter ratio (L/D) and water entry angle were investigated on the projectile stability within the cavity. Accordingly, the water entry of five projectiles were simulated with aspect ratios of 2 to 6 at three water entry angles of 6, 9 and 12 degrees with respect to the free surface and with an initial velocity of 280 m/s. The following results were obtained:

1. As the L/D decreases, the trajectory of the projectile is converted from a straight line to a curved shape and tail-slap occurs within a shorter time duration. In addition, the projectile's initial angular velocity, which is generated by making

contact with the free surface, increases. With further reduction in L/D to a critical value $(L/D)_{Cr}$, the projectile becomes unstable and tumbles inside the cavity.

2. In the cylindrical projectile at water entry angles of 6, 9 and 12 degrees, the critical L/D values are in the ranges of $4 < (L/D)_{Cr} < 5$, $3.5 < (L/D)_{Cr} < 4$ and $2 < (L/D)_{Cr} < 3$, repetitively.
3. By increasing L/D from 3 to 6, the maximum force applied to the projectile after making contact with the water surface will only increase by 5%. Therefore, it can be concluded that the change in L/D (within the range investigated in this study) has little effect on the maximum force applied to the projectile when making contact with the water surface.
4. Making contact with the free surface results in two axial and normal force components at the collision point, which, in turn, leads to an unstabilizing pitching moment on the projectile because the resultant force applied to a location out of the disk center. When the projectile is completely covered by the cavity, the only force exerted by the fluid is perpendicular to the cavitator and its location corresponds to the center of the disk.
5. The water entry causes an unstable initial angular momentum on the cylindrical projectile. This angular momentum generates an angular velocity in the projectile and causes the projectile body to collide with the cavity wall. When the normal force caused by the collision between the body and the cavity wall fails to control the initial angular velocity, the projectile becomes unstable. To achieve stable projectiles, the increase in L/D will have a significant effect to control the initial angular velocity.
6. As the water entry angle decreases, the initial angular velocity, which is generated in the projectile by making contact with the free surface, increases. This interaction is most likely due to the increase in the duration of the water entry process. Under such conditions, the projectile stability criterion, i.e. the predominance of the tail-slap moment over the initial angular momentum, is faced with problems.
7. This study showed that aluminum cylindrical projectiles in which air stability is achieved with the gyroscopic effect, a 6° water entry angle is the minimum angle with respect to the gyroscopic stability of the projectile in the air and stable motion inside the cavity, and this fact is very important from a practical point of view.

REFERENCES

- Aus der Wiesche, S. (2005). Numerical simulation of cavitation effects behind obstacles and in an automotive fuel jet pump. *Heat and mass transfer* 41(7), 615-624.
- Bodily, K. G., S. J. Carlson and T. T. Truscott

- (2014). The water entry of slender axisymmetric bodies. *Physics of Fluids* 26(7), 072108.
- Chen, C., X. Yuan, X. Liu and J. Dang (2019a). Experimental and numerical study on the oblique water-entry impact of a cavitating vehicle with a disk cavitator. *International Journal of Naval Architecture and Ocean Engineering* 11(1), 482-494.
- Chen, T., W. Huang, W. Zhang, Y. Qi and Z. Guo (2019b). Experimental investigation on trajectory stability of high-speed water entry projectiles. *Ocean Engineering* 175, 16-24.
- Derakhshanian, M. S., M. Haghdel, M. M. Alishahi and A. Haghdel (2018). Experimental and numerical investigation for a reliable simulation tool for oblique water entry problems. *Ocean Engineering* 160, 231-243.
- Gao, J., Z. Chen, W. T. Wu and X. Li (2019). Numerical Investigations on the Water Entry of Cylindrical Projectiles with Different Initial Conditions. *Applied Sciences* 9(9), 1858.
- Guo, Z. T., W. Zhang and W. Cong (2012). Experimental and theoretical study on the high-speed horizontal water entry behaviors of cylindrical projectiles. *Journal of Hydrodynamics, Ser. B* 24(2), 217-225.
- Hirt, C. W. and B. D. Nichols (1981). Volume of fluid (VOF) method for the dynamics of free boundaries. *Journal of computational physics* 39(1), 201-225.
- Hou, Z., T. Sun, X. Quan, G. Zhang, Z. Sun and Z. Zong (2018). Large eddy simulation and experimental investigation on the cavity dynamics and vortex evolution for oblique water entry of a cylinder. *Applied Ocean Research* 81, 76-92.
- Hrubes, J. (2001). High-speed imaging of supercavitating underwater projectiles. *Experiments in Fluids* 30(1), 57-64.
- Iranmanesh, A. and M. Passandideh-Fard (2017). A three-dimensional numerical approach on water entry of a horizontal circular cylinder using the volume of fluid technique. *Ocean Engineering* 130, 557-566.
- Kiceniuk, T. (1954). An experimental study of the hydrodynamic forces acting on a family of cavity-producing conical bodies of revolution inclined to the flow. CIT Hydrodynamics Report E-12.17, California Institute of Technology.
- Kulkarni, S. S. and R. Pratap (2000). Studies on the Dynamics of a Supercavitating Projectile. *Applied Mathematical Modelling* 24(2), 113-129.
- McCoy, R. (1999). *Modern exterior ballistics: The launch and flight dynamics of symmetric projectiles*, Schiffer Pub.
- Mirzaei, M., M. M. Alishahi and M. Eghtesad (2015). High-speed underwater projectiles modeling: a new empirical approach. *Journal of the Brazilian Society of Mechanical Sciences and Engineering* 37(2), 613-626.
- Nguyen, V. T., D. T. Vu, W. G. Park and C. M. Jung (2016). Navier–Stokes solver for water entry bodies with moving Chimera grid method in 6DOF motions. *Computers & Fluids* 140, 19-38.
- Nguyen, V. T., D. T. Vu, W. G. Park and Y. R. Jung (2014). Numerical analysis of water impact forces using a dual-time pseudo-compressibility method and volume-of-fluid interface tracking algorithm. *Computers & Fluids* 103, 18-33.
- Passandideh-Fard, M. and E. Roohi (2008). Transient simulations of cavitating flows using a modified volume-of-fluid (VOF) technique. *International Journal of Computational Fluid Dynamics* 22(1-2), 97-114.
- Rabiee, A., M. Alishahi, H. Emdad and B. Saranjam (2011). Experimental investigation of bounce phenomenon. *Scientia Iranica* 18(3), 416-422.
- Schnerr, G. H. and J. Sauer (2001). Physical and numerical modeling of unsteady cavitation dynamics. Fourth international conference on multiphase flow, ICMF New Orleans.
- Truscott, T., A. Techet and D. Beal (2009). Shallow angle water entry of ballistic projectiles. Proc. Cav2009. Int. Symp. Cavitation, ed. S Ceccio, Art. 100
- Yu, A., Q. Tang and D. Zhou (2019). Cavitation Evolution around a NACA0015 Hydrofoil with Different Cavitation Models Based on Level Set Method. *Applied Sciences* 9(4), 758.
- Yuan, X., C. Chen, Y. Wang and X. Liu (2017). On the cavity pressure during the water-entry of a supercavitating vehicle. *OCEANS–Anchorage*, 2017, IEEE.
- Zwart, P. J., A. G. Gerber and T. Belamri (2004). A two-phase flow model for predicting cavitation dynamics. *Fifth international conference on multiphase flow*, Yokohama, Japan.